Received: 14 November 2023 | Revised: 28 December 2023 | Accepted: 7 January 2024

DOI: 10.1111/jace.19721

Journal of the American Ceramic Society

RESEARCH ARTICLE

Isotropic negative thermal expansion in ZrW_2O_8 and HfW_2O_8 from 1100 to 1275°C

Benjamin S. Hulbert[1] | **Dylan W. Blake**[1] | **Gerard S. Mattei**[2] | **Waltraud M. Kriven**[1]

[1]Department of Materials Science and Engineering, University of Illinois at Urbana-Champaign, Urbana, Illinois, USA

[2]Department of Chemistry, State University of New York Stony Brook, Stony Brook, New York, USA

Correspondence
Waltraud M. Kriven, Department of Materials Science and Engineering, University of Illinois at Urbana-Champaign, Urbana, IL 61801, USA.
Email: kriven@illinois.edu

This work is based on chapter 4 in the doctoral dissertation: Hulbert B. S. An in situ synchrotron study of low positive and negative thermal expansion ceramics, University of Illinois Urbana-Champaign, 2023. https://hdl.handle.net/2142/121482

Funding information
National Science Foundation; Directorate for Materials Research, Grant/Award Number: 1838595

Abstract

ZrW_2O_8 (ZrO_2•$2WO_3$) and HfW_2O_8 (HfO_2•$2WO_3$) have been the focus of thermal expansion studies due to their isotropic negative thermal expansion (NTE) measured previously at temperatures below 775°C. This work presents measurements of these materials at their thermodynamically stable temperature ranges of 1105 and 1257°C for ZrW_2O_8 and 1105–1276°C for HfW_2O_8, where they were characterized with in situ, powder X-ray diffraction. The linear coefficients of thermal expansion were measured to be -5.52×10^{-6} and -4.87×10^{-6}°C^{-1} for ZrW_2O_8 and HfW_2O_8, respectively. The mechanism leading to this NTE is discussed. Powder samples were synthesized by a solution-based process called the organic–inorganic steric entrapment method. In situ characterization in air was carried out at the National Synchrotron Light Source II using a hexapole lamp, optical furnace and the Advanced Photon Source using a quadrupole lamp, optical furnace to achieve elevated temperatures.

KEYWORDS
equilibrium, HfW_2O_8, high temperature, in situ, isotropic, negative thermal expansion, synchrotron radiation, ZrW_2O_8

1 | INTRODUCTION

Zirconium tungstate, ZrW_2O_8 (ZrO_2•$2WO_3$), and hafnium tungstate, HfW_2O_8 (HfO_2•$2WO_3$), are archetypal examples of negative thermal expansion (NTE) in ceramics.[1–6] They have previously been studied primarily where they are metastable and outside of their equilibrium temperature ranges from −272.85 to 775°C.[7,8] The interest in these two materials is due to the isotropic nature of the NTE and because they exhibit NTE over a larger temperature range than most materials.[9] ZrW_2O_8 and HfW_2O_8 studies are motivated by their application in the engineered thermal expansion of composite materials[10] and recent studies[11–14] have focused on the mechanism leading to NTE. An improved understanding of the fundamental NTE mechanism could be applied to the control of thermal expansion properties of other systems. ZrW_2O_8 and HfW_2O_8 have also shown low thermal conductivity[15,16] and have been used in thermal management applications.[17]

In the binary ZrO_2–WO_3 phase diagram, Chang et al.[18] concluded that ZrW_2O_8 has a narrow stability region in that it forms only between 1105 and 1257°C at 101.3 kPa (1 atm) pressure. Below this temperature range, its phase separates into its component oxides, ZrO_2 and WO_3. Above this temperature range, it melts incongruently, forming a liquid with ZrO_2 precipitates. If it is quenched from about 1200 to 25°C, two cubic phases can persist at lower temperatures as metastable phases. The kinetics are slow enough at temperatures below about 800°C that the metastable cubic ZrW_2O_8 crystal structures persist outside of their thermodynamically stable temperature range. Previous studies have probed the thermal expansion of ZrW_2O_8 below 800°C.[3,7,8,15,16] However, Duan et al.[19] collected one neutron diffraction pattern of ZrW_2O_8 at 1170°C showing a continued unit cell contraction. HfW_2O_8 has a similar phase diagram with its stability region from 1105 to 1276°C.[18] $ZrMo_2O_8$ ($ZrO_2 \cdot 2Mo_2O_3$) has a similar structure and has NTE but at atmospheric pressure is not stable at any temperature[20]; therefore, it was not included in this study.

ZrW_2O_8 and HfW_2O_8 have an open framework structure with two related α and β phases, both in the cubic crystal system. The high-temperature β-ZrW_2O_8 crystal structure, shown in Figure 1, forms between 1105 and 1257°C and has a $Pa\bar{3}$ (*SG* 205) space group, with four formula units per unit cell.[8] This structure also exists from 164 to 775°C, where it is metastable if quenched. On cooling, there is a phase transition from the metastable β-ZrW_2O_8 to α-ZrW_2O_8 at 164°C,[21] which has a similar cubic crystal structure, $P2_13$ (*SG* 198), also having four formula units per unit cell. The crystal structure change between α and β phases is characterized by an order–disorder transition of the WO_4 tetrahedra.[7] For both phases, all six oxygens in ZrO_6 octahedra are corner sharing with oxygen atoms in WO_4 tetrahedra. However, only three of the four oxygen atoms in WO_4 tetrahedra are corner sharing with ZrO_6, whereas one oxygen has an unshared vertex on WO_4 or a terminal oxygen. The flexibility in the structure due to this terminal oxygen on the WO_4 tetrahedron, which is along the high symmetry [1 1 1] axis, is partially responsible for the NTE behavior in these materials. HfW_2O_8 is isomorphous with ZrW_2O_8,[7] and the α-HfW_2O_8 to β-HfW_2O_8 transformation occurs at 191°C.[21]

NTE in ZrW_2O_8 was initially shown by Martinek and Hummel[23] in 1961. In 1996, Mary et al.[7] published the crystal structures ZrW_2O_8 and HfW_2O_8 and measured thermal expansions from −272 to 775°C by X-ray and neutron diffraction. Since then, numerous studies have worked to determine the mechanism leading to this uncommon thermal expansion.[1] Many different types of characterization experiments and computational lattice dynamics studies have been performed, including dilatometry,[7,8,23] X-ray diffraction (XRD),[13,21] neutron diffraction,[7,24,25] X-ray pair distribution function (PDF) analysis,[12,13] neutron PDF analysis,[11] Raman spectroscopy,[7,26] X-ray absorption fine structure (XAFS),[27,28] extended XAFS (EXAFS),[12] inelastic neutron scattering (measuring phonon and Grüneisen parameters),[25,29] heat capacity,[21,30] infrared spectroscopy,[31] density functional theory calculations,[13,14,32] and other studies as summarized here.[1,33] It is important to note the following three features concerning the previous studies. There has been some disagreement about which lattice dynamics and phonon modes are responsible for the precise mechanism causing NTE. Most previous studies were completed within the temperature range from −272.85 to 775°C, and some only investigated the α phase. Additionally, it can be inferred that ZrW_2O_8 and HfW_2O_8 samples

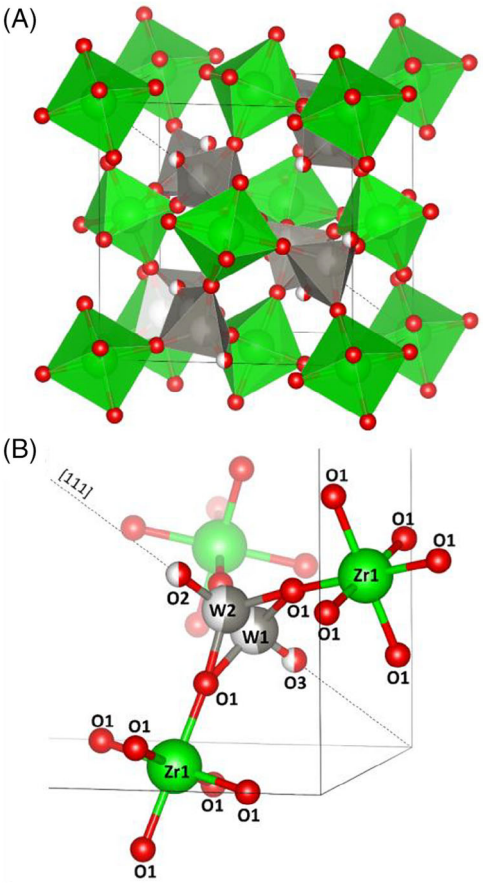

FIGURE 1 (A) Crystal structure of β-ZrW_2O_8 in the $Pa\bar{3}$ space group and (B) a selected subset of the unit cell shown with atom labels to depict the corner sharing nature of the HfO_6 octahedra and WO_4 tetrahedra. Each WO_4 tetrahedron has three of its four corners shared with ZrO_6 octahedra; oxygen atoms O_2 and O_3 are terminal vertices. O_1 located on each of the six vertices of each ZrO_6 octahedron are shared with surrounding WO_4 tetrahedra. HfW_2O_8 and ZrW_2O_8 are isomorphous; HfW_2O_8 can be visualized by replacing Zr atoms with Hf atoms. Orientations of (A) and (B) are seen from the same perspective using the program VESTA.[22]

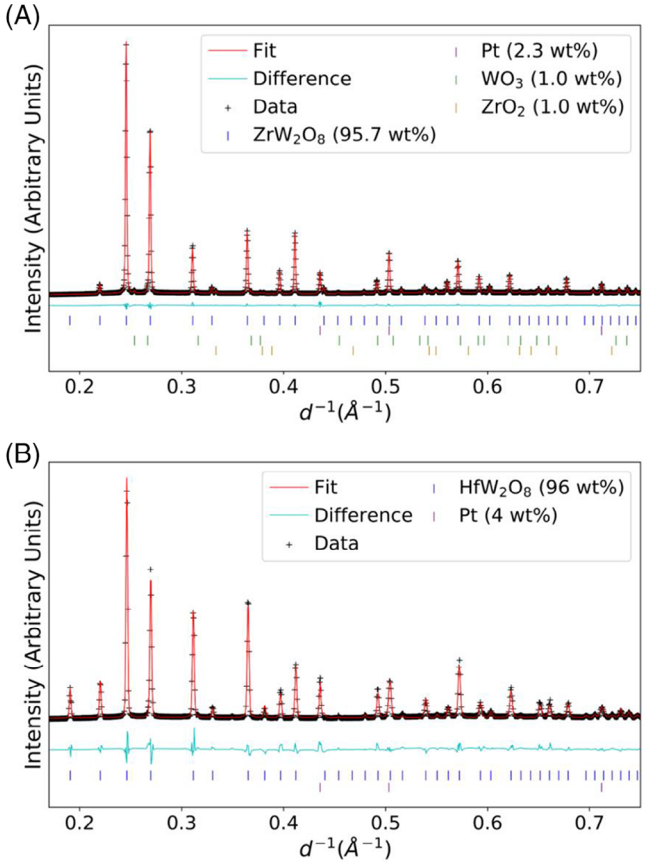

FIGURE 2 Powder diffraction patterns and Rietveld fits for (A) ZrW_2O_8 at 1210 (±2)°C and (B) HfW_2O_8 at 1209 (±4)°C both in the $Pa\bar{3}$ space group. Pt peaks were from the internal temperature standard. Corresponding crystallographic and Rietveld data can be found in Table 1. Minor phases of WO_3 and ZrO_2 in (A) formed when ZrW_2O_8 began to phase separate as it was quickly heated from 25°C to the 1100 to 1275°C temperature range. Both crystal structures were refined from the starting structures reported by Evans et al.[7]

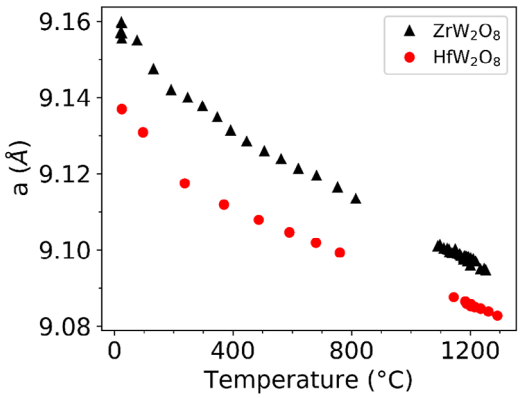

FIGURE 3 Unit cell parameter values for ZrW_2O_8 and HfW_2O_8 from 25 to 1300°C, showing negative thermal expansion at their equilibrium temperature ranges from 1100 to 1300°C. Estimated standard uncertainties are smaller than the data markers.

in many previous studies had thermal stresses and strains present from the quenching process during sample synthesis, although Yamamura et al.[21] and Evans et al.[24] had included an annealing step to mitigate against this.

This article will describe (i) a new, solution-based synthesis method for ZrW_2O_8 and HfW_2O_8, (ii) in situ XRD measurements from 25 to 1300°C with synchrotron radiation, and (iii) structural analyses via the Rietveld refinements. The purpose was to determine if β-ZrW_2O_8 and β-HfW_2O_8 continue to show NTE at their equilibrium temperature ranges as well as to determine if the thermal expansion mechanism is similar to that of the lower temperature studies.

2 | EXPERIMENTAL PROCEDURES

2.1 | Powder synthesis and preliminary characterization

Powders of ZrW_2O_8 and HfW_2O_8 were synthesized by the organic–inorganic steric entrapment method.[34–37] This involved the mixing of stoichiometric ratios of zirconium(IV) chloride, $ZrCl_4$ (98%, Sigma-Aldrich), or hafnium(IV) chloride, $HfCl_4$ (98%, Sigma-Aldrich), in water with tungsten(IV) chloride, WCl_4, (≥99.9% trace metals basis, Sigma-Aldrich) in isopropanol. Solvents for each were chosen for the ease of dissociation of the chloride salts. This solution was combined with a 5 wt% ethylene glycol, HO–CH_2–CH_2–OH (99%, Fisher Scientific), in isopropanol solution. A 1:4 ratio was kept for the number of negative hydroxyl (−OH) groups (two in each ethylene glycol molecule) to the total positive cation valence charges (Zr^{4+} or Hf^{4+} and W^{4+}). This solution was stirred continuously on a hot plate for 4 h and then heated until the isopropanol had evaporated.

The next step in the heat treatment involved placing the hot plate-dried, zirconium or hafnium (IV) chloride, tungsten (IV) chloride, and ethylene glycol mixture in a Carbolite box furnace at 200°C for 3 h with ramp rates of 5°C/min on heating and 10°C/min on cooling, followed by grinding with a mortar and pestle. A calcination step was followed at 700°C for 2 h with 2°C/min on heating and 10°C/min on cooling. This calcined powder was then pressed to 60 MPa into a 12.7 mm (0.5″) diameter pellet, placed on platinum foil in an alumina crucible and crystallized in a Teresco furnace at 1200°C for 6 h at a ramp rate of 5°C/min on heating followed by quenching in air, on cooling. The quenching process was necessary to avoid phase separation into HfO_2 and WO_3.

Sample characterization was performed using powder XRD to confirm that a single phase ZrW_2O_8 was formed without major impurities on a Siemens-Bruker D5000 with

TABLE 1 Crystallographic and Rietveld data for selected ZrW_2O_8 and HfW_2O_8.

	ZrW_2O_8					HfW_2O_8				
Crystal data										
Crystal system	Cubic					Cubic				
Space group (number)	$Pa\bar{3}$ (205)					$Pa\bar{3}$ (205)				
Z	4					4				
T (°C)	1210 (2)					1209 (4)				
a, b, c (Å)	9.09763 (3)					9.07957 (12)				
α, β, γ (°)	90					90				
Unit cell volume (Å^3)	752.984 (8)					748.51 (3)				
	Fractional coordinates					**Fractional coordinates**				
Atom site label	***x***	***y***	***Z***	**Occupancy**	**B_{eq} (Å^2)**	***x***	***y***	***z***	**Occupancy**	**B_{eq} (Å^2)**
Zr_1 or Hf_1	0	0	0	1	2.91 (6)	0	0	0	1	1.86 (7)
W_1	0.3319 (3)	0.3319 (3)	0.3319 (3)	0.476 (2)	3.77 (6)	0.3284 (5)	0.3284 (5)	0.3284 (5)	0.445 (5)	1.41 (6)
W_2	0.6101 (2)	0.6101 (2)	0.6101 (2)	0.524 (2)	3.77 (6)	0.6100 (4)	0.6100 (4)	0.6100 (4)	0.555 (5)	1.41 (6)
O_1	0.0549 (6)	0.2061 (8)	0.0741 (7)	1	6.8 (3)	0.0689 (18)	0.1857 (16)	0.107 (2)	1	5.5 (6)
O_2	0.518 (4)	0.518 (4)	0.518 (4)	0.500 (11)	7.4 (6)	0.527 (5)	0.527 (5)	0.527 (5)	0.50 (2)	2.9 (1.2)
O_3	0.2351 (16)	0.2351 (16)	0.2351 (16)	0.500 (11)	7.4 (6)	0.247 (5)	0.247 (5)	0.247 (5)	0.50 (2)	2.9 (1.2)
	ZrW_2O_8					HfW_2O_8				
Data collection										
Radiation type	X-ray					X-ray				
Beamline[c]	17 BM-B					28-ID-2				
Source, laboratory[c]	APS bending magnet, ANL					NSLS II wiggler, BNL				
λ (Å)	0.241170					0.184700				
Sample-to-detector distance (mm)	1001.8					1423.1				
d^{-1} min-d^{-1}_{max} (Å^{-1})	0.05–0.90					0.09–1.55				
Atmosphere	Air					Air				
Sample container	Fused-silica capillary					Fused-silica capillary				
Standard material for area detector image integration	CeO_2					Pt				
Heat source	Quadrupole lamp furnace					Hexapole lamp furnace				

(Continues)

TABLE 1 (Continued)

	ZrW_2O_8		HfW_2O_8
Rietveld refinement			
Computer program	TOPAS		TOPAS
Weight %–Rietveld[a]	95.66 (9)		95.81 (11)
R_{wp} (%)[b]	3.80		6.60
R_{exp} (%)[b]	1.52		0.36
R_p (%)[b]	2.74		5.02
GoF (%)[b]	2.50		18.49
R_{Bragg} [b]	0.888		2.731

[a]Remaining wt% from internal temperature standard Pt or minor phases.
[b]Values are as defined in Bruker TOPAS Software.
[c]XRD data was collected at different locations due to beam-time availability.
Abbreviations: APS, Advanced Photon Source; ANL, Argonne National Laboratory; BNL, Brookhaven National Laboratory; NSLS II, National Synchrotron Light Source II.

Cu-K_α radiation ($\lambda = 1.5418$ Å, 40 kV, and 30 mA). XRD patterns were measured via Bragg-Brentano geometry. XRF measurements on a Shimadzu ED-XRF instrument were also collected to determine the elemental composition, which is shown in Section S1.

2.2 | High-temperature synchrotron characterization

Prior to synchrotron experiments, 5–10 wt% Pt powder (0.15–0.45 μm in size, 99.9%, Sigma-Aldrich, then heat treated at 800°C for 2 h) was mixed with each sample. This Pt was added as an internal standard, enabling calculation of the sample temperature to ±5°C,[38] serving as a thermal conductor, and determination of calibration and integration parameters for the azimuthal integration of area detector images. The sample and Pt powder mixture was mounted in a 0.5 mm fused-silica capillary (Charles Supper Company) and held at the end of an alumina tube (0.6 mm ID, 1.0 mm OD, Alfa Aesar). Sapphire capillaries could not be used due to the reactivity of Al_2O_3 with HfW_2O_8 and ZrW_2O_8 above 700°C.

In situ XRD experiments were performed in air in optical furnaces at two synchrotron beamlines, due to beam-time availability. Details for each beamline are described in the following:

a. High temperatures were achieved with a quadrupole lamp optical furnace[39] at beamline 17 BM-B at the Advanced Photon Source (APS) at Argonne National Laboratory (ANL). The wavelength was 0.24117 Å (51.4062 KeV), the data was collected in a $d_{hkl}{}^{-1}$-spacing range of 0.05 to 0.90 Å^{-1}, and the sample-to-detector distance of 1001.8 mm was determined from a single LaB_6 image calibration. Each sample was rotated by a sample spinner in the goniometer at 17 BM-B. Data was collected with a 17″ × 17″ Varex 4343CT flat area detector.
b. A hexapole lamp furnace heated samples at beamline 28-ID-2 at the National Synchrotron Light Source II (NSLS II) at Brookhaven National Laboratory (BNL), where the wavelength was 0.1847 Å (67.1231 KeV). The sample-to-detector distance was 1423–1426 mm, as determined for each sample by the image calibration from internal standard Pt for each sample. Data was collected with a 16″ × 16″ flat scintillator area detector in a $d_{hkl}{}^{-1}$-spacing range of 0.09–1.55 Å^{-1}.

Area detector images were calibrated for sample-to-detector distance, beam center, tilt angle, tilt rotation, and penetration and then azimuthally integrated with

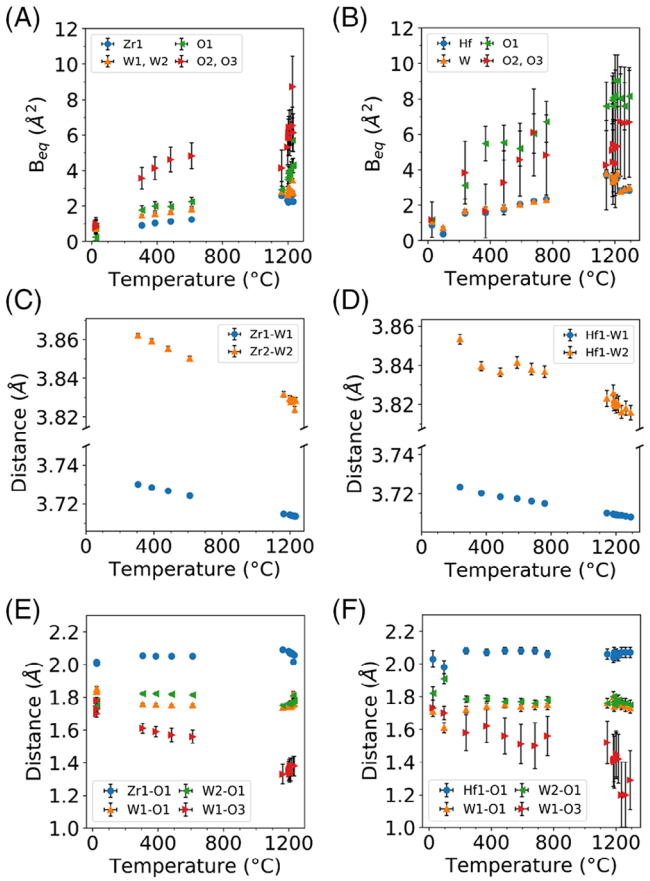

FIGURE 4 Atomic displacement parameters in (A) and (B) for ZrW_2O_8 and HfW_2O_8, respectively. Selected atom–atom distances as a function of temperature; (C) Zr–W distances; (D) Hf–W distances; cation–oxygen distances for (E) ZrW_2O_8 and (F) HfW_2O_8. Estimated standard deviations are shown for all data points, but some are smaller than the marker. Atom labels can be found in Figure 1B.

the program General Structure Analysis System II.[40] The Rietveld method[41] was used to sequentially refine the $Pa\bar{3}$ α-ZrW_2O_8 and $Pa\bar{3}$ β-HfW_2O_8 structures described by Evans et al.[7] from the temperature-dependent, XRD data with the Bruker TOPAS software.[42,43]

3 | RESULTS AND DISCUSSION

3.1 | High temperature crystal structure refinements

XRD patterns and the corresponding Rietveld fit are shown in Figure 2 for ZrW_2O_8 and HfW_2O_8 in the middle of the equilibrium temperature range at 1210°C. Structural results of ZrW_2O_8 and HfW_2O_8 at this high temperature range agreed well with the β-phase crystal structure determined by Evans et al.[7] each with low goodness of fit parameters. Crystallographic and Rietveld data for the two XRD plots are summarized in Table 1. Details describing the Rietveld refinement procedure are given in Section S2.

3.2 | Unit cell data and negative thermal expansion

The temperature-dependent, unit-cell parameters for ZrW_2O_8 and HfW_2O_8 are plotted in Figure 3. The unit cell continued to contract in the 1100 to 1275°C temperature range. Unit cell parameter values for ZrW_2O_8 and HfW_2O_8 agreed with past data from Mary et al.[8] and Yamamura et al.[21] in the regions where they overlapped. The multiple datasets in appendix C gave an estimate of the true uncertainty in the unit cell parameters from these measurements. The estimated standard deviation shown for each point each appeared smaller than the actual uncertainty, a common issue in powder XRD.[44]

The linear thermal expansion value, α_l, was calculated with Equation (1). Due to the high symmetry of the cubic crystal structures investigated, only a single value was needed to describe the expansion of the cubic unit cell. Here, the room temperature unit cell parameter, $l_{25°C}$, and a first order polynomial fit of the unit-cell parameter data for the length as a function of temperature, $l(T)$, led to a constant value for α_l in the given temperature range. Additional details on thermal expansion calculations can be found elsewhere[38,45,46]:

$$\alpha_l = \frac{1}{l_{25°C}} \frac{dl\,(T)}{dT} \tag{1}$$

In Equation (1), the linear thermal expansion coefficient, α_l, calculated from a length at 25°C, $l_{25°C}$, and a polynomial of length as a function of temperature, $l(T)$.

The linear thermal expansion was calculated for four sets of data for ZrW_2O_8 and for HfW_2O_8 and then averaged to give a single value for each material. From 1100 to 1300°C, α_l for ZrW_2O_8 was $-5.52\,(6) \times 10^{-6}°C^{-1}$, and α_l for HfW_2O_8 was $-4.87\,(11) \times 10^{-6}°C^{-1}$. α_l for β-ZrW_2O_8 and β-HfW_2O_8 reported here agreed with results from Yamamura et al.[21] from 227 to 287°C for the β phase. Values of α_l for each dataset of zirconium tungstate and hafnium tungstate can be found in Sections S3 and S4, respectively.

The change in unit cell parameter slopes in Figure 3 between 150 and 200°C corresponds to the α to β phase transformations, described previously.[8,21] The temperature was held for approximately 2 min at each temperature before a diffraction pattern was collected. This time may not have been long enough at low temperatures for equilibration. However, because there was no significant difference in unit cell parameter values when data was obtained on heating and on cooling, it could be concluded that in

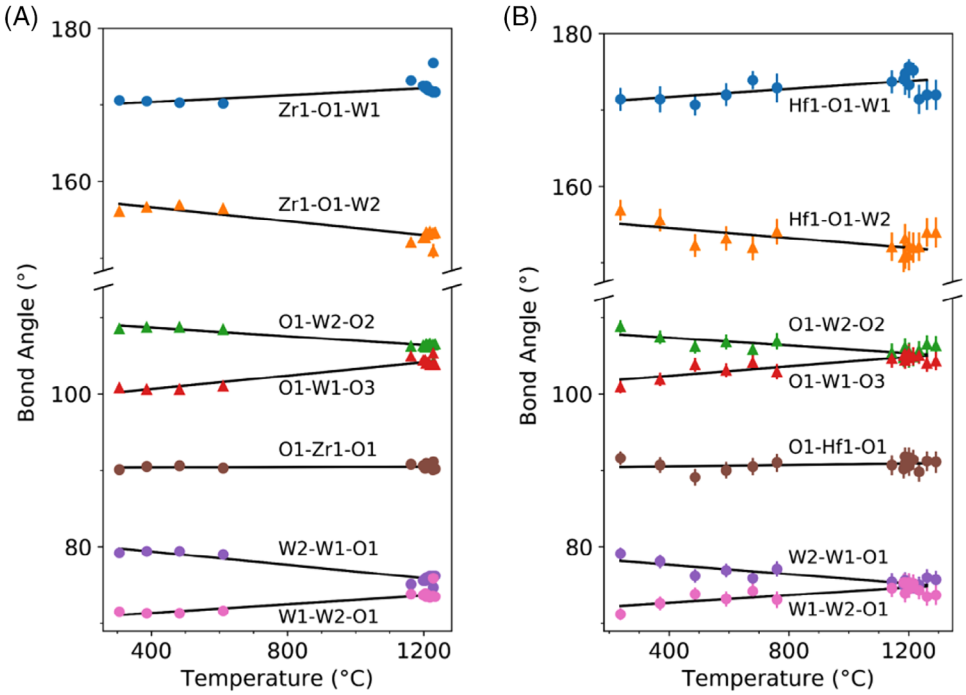

FIGURE 5 Selected bond angles as a function of temperature for (A) ZrW_2O_8 and (B) HfW_2O_8 in the $Pa\bar{3}$ space group. Black lines show a first order polynomial fit for each dataset. Atom labels are shown in Figure 1.

these high temperature experiments, there is no issue with annealing leading to structural changes as described by Evans et al.[24]

3.3 | Thermal expansion mechanism

In both the α and β phases, the WO_4 tetrahedra lie along the [111] direction, the difference being that they are disordered in the β phase. With this in mind, the thermal expansion mechanism in each temperature range (as well as crystal structure) could be compared. Selected atomic displacement parameters (B_{eq}) and atom-to-atom distances, as determined from Rietveld refinement of both ZrW_2O_8 and HfW_2O_8 structures, are shown in Figure 4. The same trends are seen in the changes in unit cell for both ZrW_2O_8 and HfW_2O_8, but they are described in terms of ZrW_2O_8 below.

The Zr_1–W_1 and Zr_2–W_2 distances both decrease with increasing temperature as the unit cell contracts. The increase in Zr_1–O_1–W_1 and O_1–W_1–O_3 angles as well as the decrease in Zr_1–O_1–W_2 and O_1–W_2–O_2 angles in Figure 5 are consistent with this contraction of the distance of the WO_4 tetrahedra along the [111] direction relative to the ZrO_6 octahedra. The W_1–O_3 distance is the only cation–oxygen bond length that appears to change length, where NTE can be seen in Figure 4E,F. W_1–O_3 is the terminal oxygen bond, and although it appears to have a shorter bond length at higher temperatures, this is likely due to transverse vibrations that lead to a measured contraction of the bond length, whereas the W–O, Hf–O, and Zr–O bonds were rigid with temperature.[47] This measured contraction of the W–O_3 bond can be interpreted as greater vibration perpendicular to the bond direction, not a decrease in bond length.[7,47,48] This is consistent with lower temperature studies that show that the NTE mechanism comes from the flexibility and vibrations of WO_4 tetrahedra.[11–13,28]

The B_{eq} values increased with temperature for all atoms due to the increased thermal vibration. B_{eq} values were largest for the lighter atoms, O_1, O_2, and O_3, as expected. However, even though the tungsten atoms were the heaviest in this system, they had larger B_{eq} values than both zirconium and hafnium atoms. This was likely due to the inherent static disorder in the β-ZrW_2O_8 structure. Both the increased B_{eq} of light atoms as well as the increased vibrations at high temperatures make the thermal expansion mechanism more difficult to determine and have been an important aspect of mechanisms presented in studies of the α-phase.[11,12] Atomic displacement parameters were refined isotropically, as they generally cannot be refined anisotropically for powder XRD data.[49] However, a powder neutron diffraction study[24] found that refining displacement parameters anisotropically led to differing bond angles when compared with an isotropic model for the same data. This would be an opportunity for additional studies in which anisotropic displacement parameters could be found.

The large temperature range measured here of β-ZrW_2O_8 and β-HfW_2O_8 made it possible to see trends in bond angles and atom-to-atom distances which were not distinguishable in previous powder XRD experiments over more limited temperature ranges. This data suggests that the NTE mechanism in this temperature range comes from translations of the WO_4 tetrahedra along the [111] direction as well as small rotations of the HfO_6 and WO_4 polyhedra. This was consistent with mechanisms of NTE found previously in lower temperature experiments.[12] Experiments in the 1100–1300°C temperature range with additional techniques such as X-ray PDF, neutron PDF, EXAFS, or infrared spectroscopy could more accurately describe the local structure and low energy phonon modes of this system.

For each dataset in this article, there is a corresponding diffraction pattern file (.xye), TOPAS output file (.out), and a crystallographic information format file (.cif) found in an online repository at the hyperlink given in the Supporting Information Section. Tabulated unit-cell parameter data is also included in the Supporting Information section.

4 | CONCLUSION

It was shown that ZrW_2O_8 and HfW_2O_8 have NTEs over the entire range at which they are thermodynamically stable from 1105 to 1257 and 1105 to 1276°C, respectively, expanding upon previous studies from −272.85 to 775°C where they are metastable. At their equilibrium temperature ranges, ZrW_2O_8 and HfW_2O_8 still showed NTE. The thermal expansion values measured here from 1100 to 1250°C for ZrW_2O_8 were $-5.52 \times 10^{-6}°C^{-1}$ and from 1100 to 1275°C for HfW_2O_8 were $-4.87 \times 10^{-6}°C^{-1}$. The thermal expansion coefficient was found to be constant over this temperature range. The mechanism of NTE appears to be similar to previous lower temperature studies in which a decrease in the distance between HfO_6 and WO_4 polyhedra along the [111] direction due to transverse vibrational modes leading to an average decrease in the HfO_6 and WO_4 polyhedra and a decrease in W_1–O_3 distance occur. HfW_2O_8 has NTE over the largest temperature range yet studied. Previously, it showed NTE at all temperatures below 775°C.

5 | RELATED LITERATURE

The following references are cited in the Supporting Information section.[40,42,43,49–53]

ACKNOWLEDGMENTS

The following funding is acknowledged: National Science Foundation, Directorate for Materials Research (Grant Number 1838595 to WMK). Use of the Advanced Photon Source was supported by the U S Department of Energy, Office of Science, Office of Basic Energy Sciences, under Contract No. DE-AC02-06CH11357 and was completed at beamline 17 BM-B. This research used resources of Beamline 28 ID-2 at the National Synchrotron Light Source II, a US Department of Energy (DOE) Office of Science User Facility operated for the DOE Office of Science by Brookhaven National Laboratory under Contract No. DE-SC0012704. The technical assistance of beam line scientists and staff, Dr. Wenqian Xu and Dr. Andrey Yakovenko at the APS, ANL, as well as Dr. Sanjit Ghose, Dr. Jian Min Bai, and John Trunk at NSLS II, BNL is gratefully acknowledged. Additionally, the authors thank Kuo-Pin Tseng and Julia E. Brodecki who assisted with the beamline experiments.

ORCID

Benjamin S. Hulbert https://orcid.org/0000-0001-8098-0026

Waltraud M. Kriven https://orcid.org/0000-0002-2983-5760

REFERENCES

1. Petrushina MY, Korenev SV, Dedova ES, Gubanov AI. Materials AM_2O_8 (A = Zr, Hf; M = W, Mo) with negative thermal expansion. J Struct Chem. 2020;61(11):1655–80.
2. Lind C. Two decades of negative thermal expansion research: where do we stand? Materials (Basel). 2012;5(12):1125–54.
3. Romao CP, Miller KJ, Whitman CA, White MA, Marinkovic BA. Negative thermal expansion (thermomiotic) materials. In Comprehensive inorganic chemistry II from elements to applications. 2nd ed. Amsterdam: Elsevier; 2013. p. 127–51.
4. Dove MT, Fang H. Negative thermal expansion and associated anomalous physical properties: review of the lattice dynamics theoretical foundation. Reports Prog Phys. 2016;79:1–50.
5. Takenaka K. Progress of research in negative thermal expansion materials: paradigm shift in the control of thermal expansion. Front Chem. 2018;6(267):1–13.
6. Evans JSO. Negative thermal expansion materials†. J Chem Soc Dalt Trans. 1999;(19):3317–26.
7. Evans JSO, Mary TA, Vogt T, Subramanian MA, Sleight AW. Negative thermal expansion in ZrW_2O_8 and HfW_2O_8. Chem Mater. 1996;8(12):2809–23.
8. Mary TA, Evans JSO, Vogt T, Sleight AW. Negative thermal expansion from 0.3 to 1050 Kelvin in ZrW_2O_8. Science. 1996;272(5258):90–92.
9. Coates CS, Goodwin AL. How to quantify isotropic negative thermal expansion: magnitude, range, or both? Mater Horizons. 2019;6(2):211–18.
10. Lommens P, De Meyer C, Bruneel E, De Buysser K, Van Driessche I, Hoste S. Synthesis and thermal expansion of ZrO_2/ZrW_2O_8 composites. J Eur Ceram Soc. 2005;25(16):3605–10.
11. Tucker MG, Goodwin AL, Dove MT, Keen DA, Wells SA, Evans JSO. Negative thermal expansion in ZrW_2O_8:

mechanisms, rigid unit modes, and neutron total scattering. Phys Rev Lett. 2005;95(25):255501.
12. Bridges F, Keiber T, Juhas P, Billinge SJL, Sutton L, Wilde J, et al. Local vibrations and negative thermal expansion in ZrW_2O_8. Phys Rev Lett. 2014;112(4):045505.
13. Baise M, Maffettone PM, Trousselet F, Funnell NP, Coudert FX, Goodwin AL. Negative hydration expansion in ZrW_2O_8: microscopic mechanism, spaghetti dynamics, and negative thermal expansion. Phys Rev Lett. 2018;120(26):265501.
14. Rimmer LHN, Refson K, Dove MT. Phonon mechanism for the negative thermal expansion of zirconium tungstate, ZrW_2O_8. Phys Chem Chem Phys. 2023;25(25):16753–62.
15. Tanusilp S, Kumagai M, Ohishi Y, Furusawa H, Suwabe M, Kurosaki K. Ultralow thermal conductivity of highly dense ZrW2O8 ceramics with negative thermal expansion. Adv Eng Mater. 2022;24:2101720.
16. Kennedy CA, White MA. Unusual thermal conductivity of the negative thermal expansion material, ZrW_2O_8. Solid State Commun. 2005;134(4):271–76.
17. Holzer H, Dunand DC. Phase transformation and thermal expansion of Cu/ZrW_2O_8 metal matrix composites. J Mater Res. 1999;14(3):780–89.
18. Chang LLY, Scroger MG, Phillips B. Condensed phase relations in the systems ZrO_2–WO_2–WO_3 and HfO_2–WO_2–WO_3. J Am Ceram Soc. 1967;50(4):211–15.
19. Duan N, Kameswari U, Sleight AW. Further contraction of ZrW_2O_8. J Am Chem Soc. 1999;121(44):10432–33.
20. Lind C, Wilkinson AP, Hu Z, Short S, Jorgensen JD. Synthesis and properties of the negative thermal expansion material cubic $ZrMo_2O_8$. Chem Mater. 1998;10(9):2335–37.
21. Yamamura Y, Nakajima N, Tsuji T. Calorimetric and X-ray diffraction studies of α-to-β structural phase transitions in HfW_2O_8 and ZrW_2O_8. Phys Rev B. 2001;64(18):184109.
22. Momma K, Izumi F. VESTA: a three-dimensional visualization system for electronic and structural analysis. J Appl Crystallogr. 2008;41(3):653–58.
23. Martinek C, Hummel FA. Linear thermal expansion of three tungstates. J Am Ceram Soc. 1968;51(4):227–28.
24. Evans JSO, David WIF, Sleight AW. Structural investigation of the negative-thermal-expansion material ZrW_2O_8. Acta Crystallogr Sect B Struct Sci Cryst Eng Mater. 1999;55(3):333–40.
25. Ernst G, Broholm C, Kowach GR, Ramirez AP. Phonon density of states and negative thermal expansion in ZrW_2O_8. Nature. 1998;396(6707):147–49.
26. Liang EJ, Liang Y, Zhao Y, Liu J, Jiang Y. Low-frequency phonon modes and negative thermal expansion in $A(MO_4)_2$ (A = Zr, Hf and M = W, Mo) by Raman and terahertz time-domain spectroscopy. J Phys Chem A. 2008;112(49):12582–87.
27. Cao D, Bridges F, Kowach GR, Ramirez AP. Frustrated soft modes and negative thermal expansion in ZrW_2O_8. Phys Rev Lett. 2002;89(21):215902.
28. Cao D, Bridges F, Kowach GR, Ramirez AP. Correlated atomic motions in the negative thermal expansion material ZrW_2O_8: a local structure study. Phys Rev B. 2003;68(1):014303.
29. Mittal R, Chaplot SL, Kolesnikov AI, Loong CK, Mary TA. Inelastic neutron scattering and lattice dynamical calculation of negative thermal expansion in HfW_2O_8. Phys Rev B. 2003;68(5):054302.
30. Yamamura Y, Nakajima N, Tsuji T, Iwasa Y, Saito K, Sorai M. Heat capacity and grüneisen function of negative thermal expansion compound HfW_2O_8. Solid State Commun. 2002;121(4):213–17.
31. Hancock JN, Turpen C, Schlesinger Z, Kowach GR, Ramirez AP. Unusual low-energy phonon dynamics in the negative thermal expansion compound ZrW_2O_8. Phys Rev Lett. 2004;93(22):225501.
32. Gava V, Martinotto AL, Perottoni CA. First-principles mode Grüneisen parameters and negative thermal expansion in α-ZrW_2O_8. Phys Rev Lett. 2012;109(19):195503.
33. Barrera GD, Bruno JAO, Barron THK, Allan NL. Negative thermal expansion. J Phys Condens Matter. 2005;17(4):R217.
34. Nguyen MH, Lee SJ, Kriven WM. Synthesis of oxide powders by way of a polymeric steric entrapment precursor route. J Mater Res. 1999;14(8):3417–26.
35. Ribero D, Kriven WM. Synthesis of $LiFePO_4$ powder by the organic-inorganic steric entrapment method. J Mater Res. 2015;30(14):2133–43.
36. Gülgün MA, Nguyen MH, Kriven WM. Polymerized organic-inorganic synthesis of mixed oxides. J Am Ceram Soc. 1999;82(3):556–60.
37. Gülgün MA, Kriven WM, Nguyen MH. Processes for preparing mixed-oxide powders. USA: United States Patent: US6482387 B1, 2002. http://www.google.ch/patents/US6482387
38. Touloukian YS. Thermal expansion: metallic elements and alloys. In Thermophysical properties of matter. vol. 12. New York: IFI/Plenum; 1975;254–59.
39. Sarin P, Yoon W, Jurkschat K, Zschack P, Kriven WM. Quadrupole lamp furnace for high temperature (up to 2050 K) synchrotron powder X-ray diffraction studies in air in reflection geometry. Rev Sci Instrum. 2006;77(9):093906.
40. Toby BH, Von Dreele RB. GSAS-II: the genesis of a modern open-source all purpose crystallography software package. J Appl Crystallogr. 2013;46(2):544–49.
41. Rietveld HM. A profile refinement method for nuclear and magnetic structures. J Appl Crystallogr. 1969;2(2):65–71.
42. Bruker. TOPAS: general profile and structure analysis software for powder diffraction data. Karlsruhe, Germany: Bruker AXS; 2007.
43. Coelho AA. TOPAS and TOPAS-academic: an optimization program integrating computer algebra and crystallographic objects written in C++. J Appl Crystallogr. 2018;51(1):210–18.
44. David WIF. Powder diffraction: least-squares and beyond. J Res Natl Inst Stand Technol. 2004;109(1):107.
45. Taylor R. Thermal Expansion of Solids, CINDAS data series on materials properties. Materials Park, OH: ASM International; 1998.
46. Schlenker JL, Gibbs GV, Boisen MB. Thermal expansion coefficients for monoclinic crystals: a phenomenological approach. Am Mineral. 1975;60:828–33.
47. Hazen R, Prewitt C. Effects of temperature and pressure on interatomic distances in oxygen-based minerals. Am Mineral. 1977;62(3–4):309–12.
48. Downs RT, Gibbs GV, Bartelmehs KL, Boisen MB. Variation of bond lengths and volumes of silicate tetrahedra with temperature. Am Mineral. 1992;77(7–8):751–57.

49. McCusker LB, Von Dreele RB, Cox DE, Louër D, Scardi P. Rietveld refinement guidelines. J Appl Crystallogr. 1999;32(1):36–50.
50. Hill RJ. Rietveld refinement round Robin. I. Analysis of standard X-Ray and neutron data for $PbSO_4$. J Appl Crystallogr. 1992;25(5):589–610.
51. Hill RJ, Cranswick LMD. International union of crystallography. Commission on powder diffraction. Rietveld refinement round Robin. II. Analysis of monoclinic ZrO_2. J Appl Crystallogr. 1994;27(5):802–44.
52. Dinnebier RE, Leineweber A, Evans JSO. Rietveld refinement: practical powder diffraction pattern analysis using TOPAS. 1st ed. Berlin, Boston: De Gruyter; 2018.
53. Hulbert BS, Kriven WM. Specimen-displacement correction for powder X-ray diffraction in Debye–Scherrer geometry with a flat area detector. J Appl Crystallogr. 2023;56(1):160–66.

SUPPORTING INFORMATION

Additional supporting information can be found online in the Supporting Information section at the end of this article.

How to cite this article: Hulbert BS, Blake DW, Mattei GS, Kriven WM. Isotropic negative thermal expansion in ZrW_2O_8 and HfW_2O_8 from 1100 to 1275°C. J Am Ceram Soc. 2024;107:4594–603. https://doi.org/10.1111/jace.19721